Supplementary Information (SI) for Journal of Materials Chemistry A.

# Supplementary Information

# Robust integration of p-MXene ink with bacterial cellulose-reinforced polymer enables dynamic interaction of superior electromagnetic shielding and sensing

Danyu Liu,‡[a] Pan Xue,‡[b] Jingli Zhang,[a] Yingjia Tong,[c] Yixuan Zhang,[d] Yajing Yu,[a] Qingda Zhang,[a] Mengfei Huang,[a] Yiheng Gao,[a] Jie Li,[e] Qufu Wei[a] and Pengfei Lv*[a, e]

**Affiliations**

[a] Key Laboratory of Eco-Textiles, Ministry of Education, Jiangnan University, Wuxi 214122, Jiangsu P. R. China

[b] Xi'an Rare Metal Materials Institute Co. Ltd, Xi'an 710016, P. R. China

[c] School of Life Sciences and Health Engineering, Jiangnan University, Wuxi 214122, Jiangsu, P. R. China

[d] Wuxi Maternityand Child Health Care Hospital, Women's Hospital of Jiangnan University, Jiangnan University,Wuxi 214002, P. R. China

[e] Jiangsu Textiles Quality Services Inspection Testing Institute, Nanjing 210007, P. R. China.

*Corresponding author. E-mail: pengfeilv@jiangnan.edu.cn (P.F. Lv)

## Content

# 1. Supplementary Figures and Results

## 1.1 Characterizations of p-MXene ink and WPU/BC film

The rheological properties of the inks were measured with a TA Instruments DHR-3 flat plate rheometer at 25 °C. The viscosity change as a function of shear rate was measured at shear rates between 0.01 to 100 $s^{-1}$ using logarithmic steps. The viscoelastic properties of the inks were studied by measuring the storage modulus (G') and loss modulus (G") of the viscoelastic energy of the ink as a function of frequency at a constant strain amplitude of 0.1%. Among them, p-MXene inks deliver much higher frequency-independent storage modulus (G') and loss modulus (G") than MXene ink (**Fig S1**), implying the formation of a pseudo solid network.[1] The high elasticity and viscosity of p-MXene ink enable the rapid formation of high-resolution, complex patterns.

In Fourier-transform infrared (FT-IR) spectra (**Fig. S2**), compare with MXene, p-$MXene_{10}$ shows additional aromatic and nitrogenous species that are widely present in polyphenols, for example, the N-H bending mode of aromatic secondary amine (1470 $cm^{-1}$) and C-N stretching of the quinoid ring (1260 $cm^{-1}$) in the FT-IR spectrum.[2]

In the X-ray diffraction (XRD) pattern (**Fig. S3**), transformation of the material is clearly presented. The sharp peaks at 6.9°, 14.0°, and 28.4° of MXene film can match well with the (002), (004) and (008) characteristic crystal planes of $Ti_3C_2T_x$, proving the transformation from MAX phase to MXene.

Furthermore, XPS analysis was conducted to explore the mechanism of DA oxidative polymerization in the preparation of p-MXene.[2] The catechol groups in DA and its derivatives have a strong affinity for multivalent metal ions through coordination bonds, especially with titanium oxide, which has been widely studied. In comparison to MXene, the XPS spectrum of p-$MXene_{10}$ reveals the presence of nitrogen (**Fig. S4a**), in addition to C, O, Ti, and F, indicating the successful incorporation of PDA. The high-resolution C1s spectrum of p-$MXene_{10}$ shows a distinct peak at 288.7 eV (**Fig. S4b**), indicating the presence of catechol-Ti coordination bonds (denoted as C-O-Ti). The C-Ti and C-Ti-Tx peaks shift towards lower binding energies, suggesting an electron transfer from PDA to MXene. The high-resolution O1s spectrum of p-MXene-10 reveals the presence of quinone (C-O) at 531.4 eV (**Fig. S4c**), which may overlap with the peak corresponding to the C-O-Ti bond. Additionally, the binding energies of the C-Ti-Tx (with Tx representing surface hydroxyl and oxygen groups) and Ti-O peaks decrease slightly, likely due to interfacial electron transfer induced by the dehydration of MXene's surface hydroxyls in conjunction with chol. As shown in **Fig. S4d**, the high-resolution N 1s spectrum of p-MXene$_{10}$ displays three peaks at 400.0, 398.7, and 396.0 eV, corresponding to R-NH-R, R=N-R, and N-Ti bonds, indicating the occurrence of DA oxidative polymerization and the binding of DA to the MXene surface. **Fig. S5** demonstrates the oxidation of pure MXene and modified MXene after being left for a week, and it can be seen that PDA effectively slows down the oxidation of MXene.

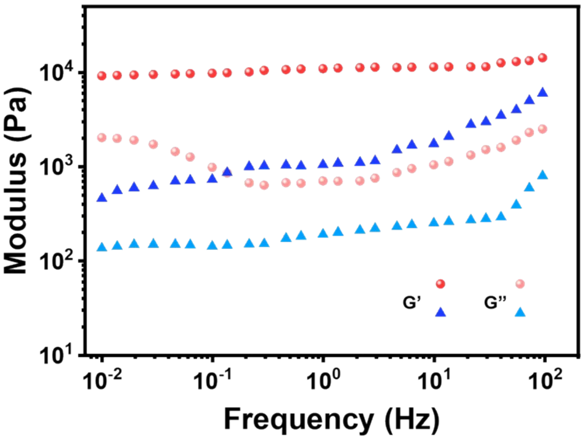

**Fig. S1.** the dependence of storage and loss moduli on frequency.

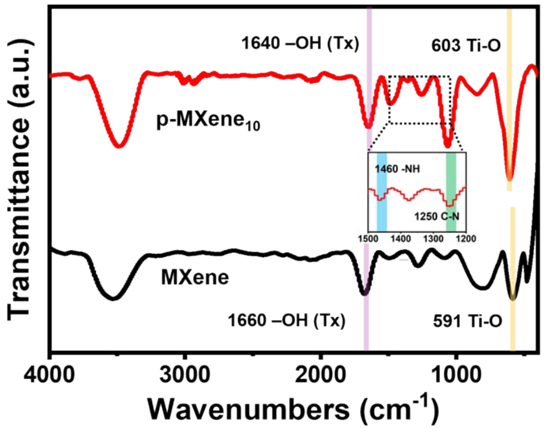

**Fig. S2.** MXene and p-MXene$_{10}$ FT-IR spectra.

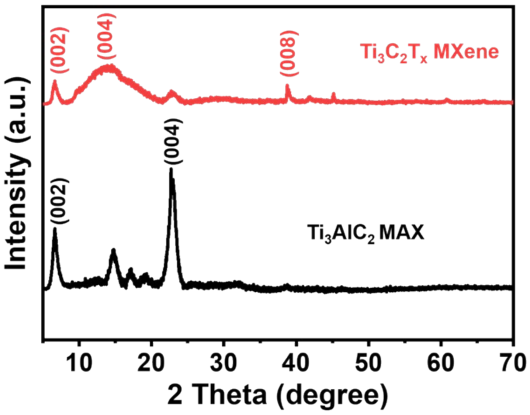

**Fig. S3.** XRD image of MXene and p-MXene.

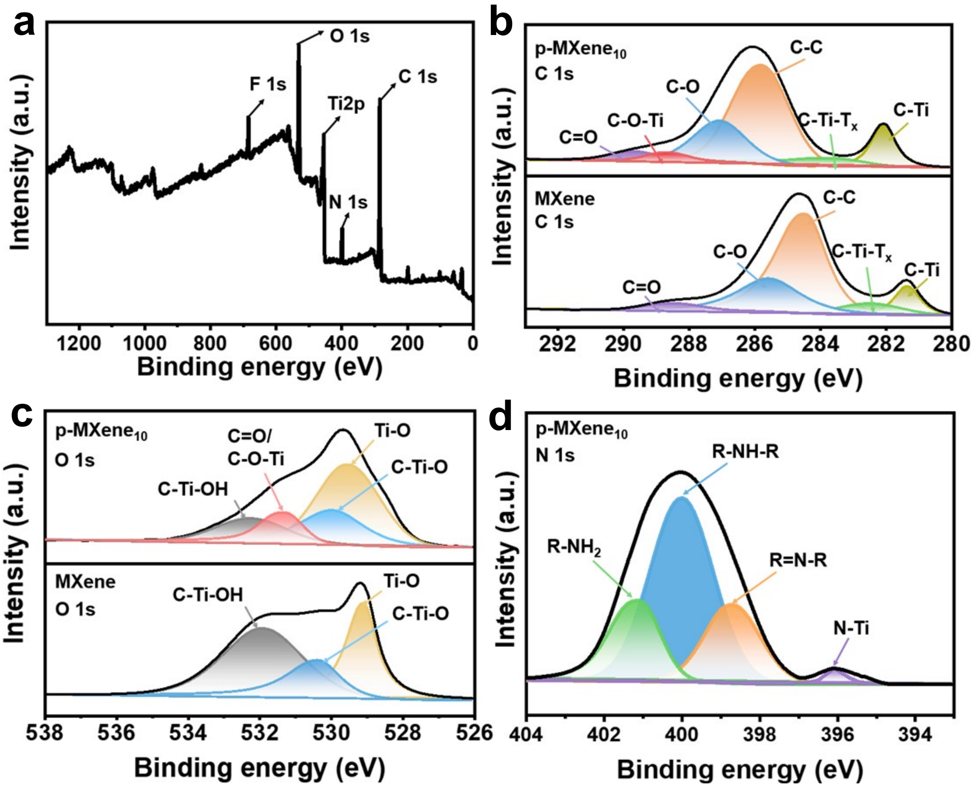

**Fig. S4.** X-ray photoelectron spectroscopy (XPS) of MXene nano monomer.

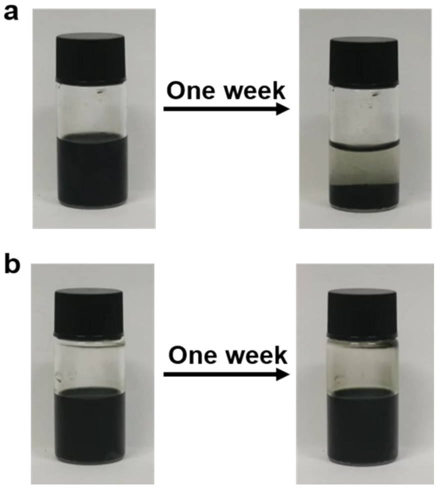

**Fig. S5.** Photographs of (a) MXene and (b) p-MXene placed for a week.

### 1.2 Synthesis and characterizations of p-MXene@WPU/BC composite film

The mechanical behavior of neat BC, 9% WPU/BC, 12% WPU/BC and 32% WPU/BC was evaluated by stress-strain curves are gathered in **Fig. S6**. The experimental data demonstrate that the composites exhibit enhanced mechanical properties with increasing WPU concentration. There is a significant increase in fracture strength and maximum elongation. Consequently, when subjected to external forces, the BC composites with a higher percentage of WPU are able to withstand greater tensile forces without fracture and experience greater deformation before failure. These findings suggest that the function of WPU as a plasticizer or reinforcing agent is pivotal in enhancing the flexibility and tensile strength of the BC matrix. Notably, the composites demonstrated optimal combined mechanical properties at a WPU proportion of 32%, and this concentration was utilized subsequently unless otherwise specified.

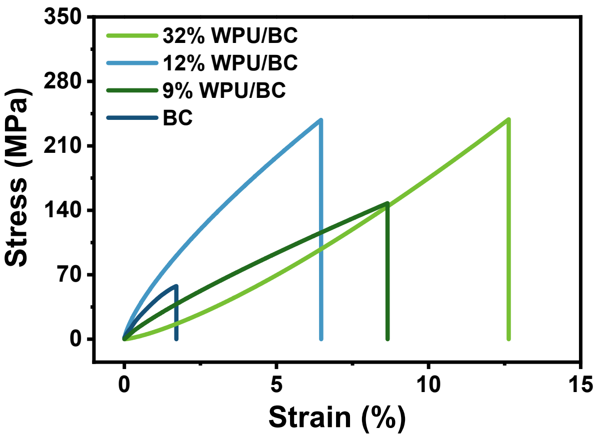

**Fig. S6.** Stress-strain curves of 32%WPU/BC, 12%WPU/BC, 9%WPU/BC and BC.

The SEM image shows the 3D fiber network structure of BC in the interior. (**Fig. S7**) To identify the possible interactions between BC and WPU in the nanocomposites, FTIR spectroscopy analysis was carried out. In **Fig. S8**, the FTIR spectra of BC, WPU and WPU/BC are shown (FTIR spectra of the other nanocomposites were almost identical to the one presented). The neat WPU showed the typical bands of the repetitive urethane group (-NHCOO-). The band located at 3450 cm$^{-1}$ corresponds to stretching vibration of N-H bond. The bands at 2960 and 2870 cm$^{-1}$ are associated to stretching vibration of C–H. The characteristic band about 1730 cm$^{-1}$ is related with the urethane C=O group. The band at 1140 cm$^{-1}$ corresponds to asymmetric stretching vibration of C-O.[3,4] In the case of BC membrane, the broad band around 3340 cm$^{-1}$ corresponds to O-H cellulose stretching vibrations. The absorption bands at 2960-2860 and 1430 cm$^{-1}$ are assigned to the CH and $CH_2$ stretching and bending vibrations, respectively. The C-O-C bond of the glycosidic bridges corresponds to the bands at 1000 cm$^{-1}$, while the band at 900 cm$^{-1}$ is characteristic of $\beta$-linked glucose-based polymers.[5] In the nanocomposite spectrum, the peaks of the BC are not observed due to the high content and coating of WPU.

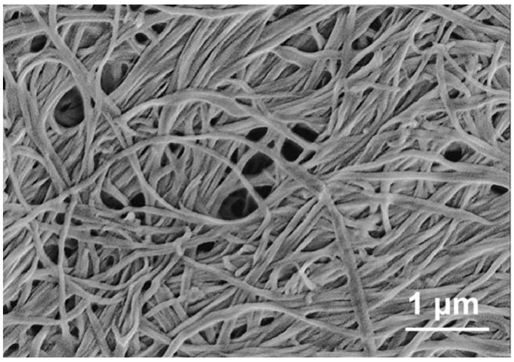

**Fig. S7.** SEM images of internal BC network structure.

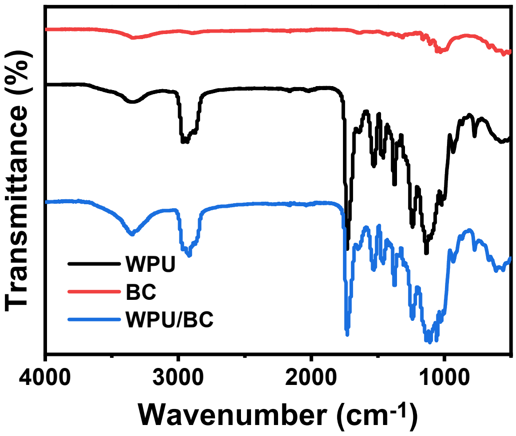

**Fig. S8.** The FTIR spectra of WPU, BC and WPU/BC composite film.

### 1.3 Mechanical properties of p-MXene@WPU/BC film

It is observed a rise in elongation at break of the nanocomposites due to the surface coating p-MXene ink, the toughness and modulus of the nanocomposites experienced an improvement with respect to the neat WPU/BC (**Fig. S9**). This enhancement can be attributed to the high strength of the p-MXene layer and the strong interfacial interactions formed between it and the matrix. p-MXene enhances the material's mechanical properties and promotes efficient transfer of stresses through improved interfacial bonding, thus increasing the material's overall mechanical strength and toughness. Furthermore, the photographs demonstrate that these films exhibit excellent folding capabilities (**Fig. S10**), maintaining structural integrity and functional stability even after multiple folding and unfolding cycles. Compared with previously reported sensing materials in terms of mechanical properties, electrical properties and electromagnetic shielding properties (**Fig. S11**). As is shown in **Fig. S12**, further exploring the mechanism of the excellent mechanical properties, BC with a complete 3D network structure is thoroughly fused with WPU, which significantly enhances the mechanical properties of the WPU matrix, thus dramatically increasing the mechanical strength of the p-MXene@WPU/BC composites.

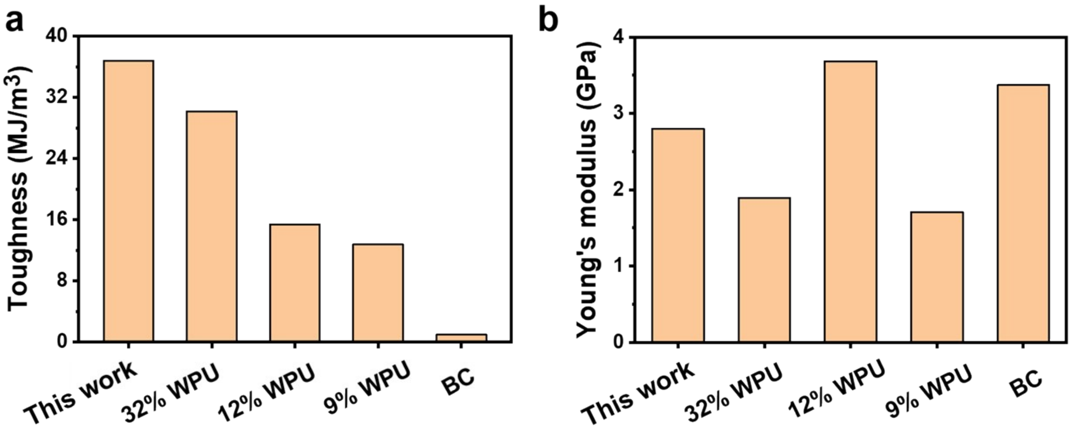

**Fig. S9.** Toughness (a) and Young's modulus (b) diagram of p-MXene@WPU/BC film, 32%WPU/BC film, 12%WPU/BC film, 9%WPU/BC film, BC film.

**Fig. S10.** Photographs showing the foldability.

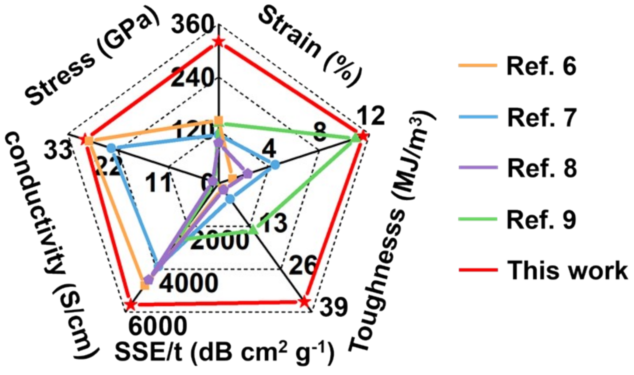

**Fig. S11.** Comparison of p-MXene5@WPU/BC composite film with previously reported sensing materials.[6–9]

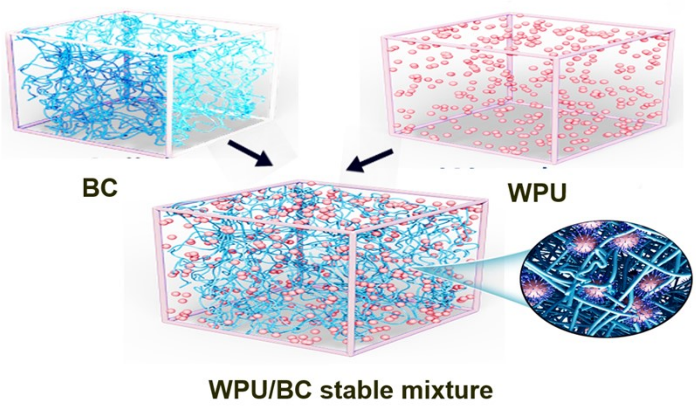

**Fig. S12.** Mechanical properties mechanism diagram.

### 1.4 Electromagnetic Shielding Properties of p-MXene@WPU/BC film

As shown in **Fig. S13**, the comparative EMI shielding effectiveness graph reveals the performance advantages of the novel composite P-MXene@WPU/BC with thickness dependence. At a fixed thickness, the total shielding effectiveness (SET) of this material (40 μm) is as high as 60 dB, which is significantly better than that of the comparison group P/WPU (20-40 dB), with the contribution of the absorptive component (SEA) accounting for about 83% (50 dB), while the reflective component (SER) is only 10 dB, suggesting that the shielding mechanism is dominated by the internal electromagnetic loss of the material. The shielding mechanism is dominated by the internal electromagnetic loss of the material. (**Fig. S13a**) As the thickness is thinned, the SET decreases sharply from 66 dB at 1000 μm to 34 dB at 80 μm, but the absorption loss (SEA) always dominates (SEA=45 dB at 1000 μm, SEA=28 dB at 80 μm), and the material maintains high shielding effectiveness (SET=34 dB) under the ultrathin (80 μm) condition. (**Fig. S13b**) The stability of the preparation process (error line ±3dB) still needs to be further improved by coating uniformity optimization.

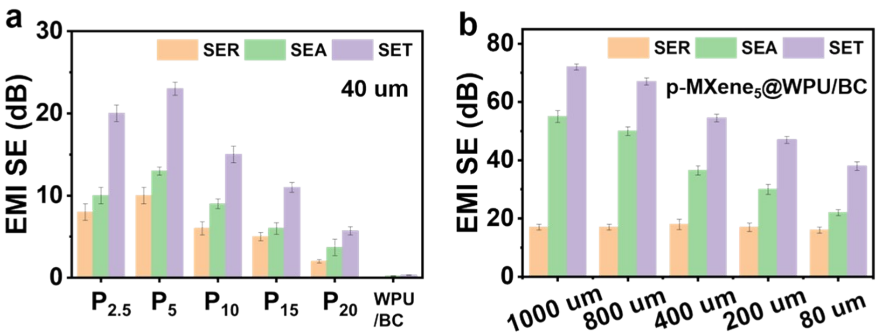

**Fig. S13** Average $SE_R$, $SE_A$, $SE_T$ values of p-MXene$_5$@WPU/BC films with (a) different PDA contents and (b) different thicknesses.

**Table S1**. Comparison of p-MXene5@WPU/BC composite film with previously reported EMI shielding materials.

| Materials | Thicknesses (mm) | SSE/t | Ref. |
|---|---|---|---|
| Carbon | 0.2 | 1250 | [10] |
| Phthalonitrile-Based Carbon | 0.2 | 1705 | [11] |
| Cu-Ni/CNTs | 0.15 | 1580 | [12] |
| CNWs/G-PDMS | 0.16 | 2319 | [13] |
| Graphene/PDMS | 0.1 | 3330 | [14] |
| rGO/Fe3O4/PEI | 0.03 | 1033 | [15] |
| rGO/PEDOT | 0.08 | 841 | [16] |
| d-$Ti_3C_2Tx$/CNFs | 0.047 | 2647 | [17] |
| MXene-TOCNF | 0.038 | 4758 | [18] |
| MXene-HA | 0.0216 | 2108 | [19] |
| **p-MXene@WPU/BC** | **0.004** | **5657** | **This work** |

### 1.5 Sensing properties of p-MXene@WPU/BC film

As shown in **Fig. S14a**, the I-V curve from -15V to 15V presents a linear relationship with the applied pressure, the slope increases and the resistance decreases. **Fig. S14(b-f)** shows that as the applied pressure increases, the on/off ratio of the current increases significantly, showing a pattern consistent with the described I-V curve. In 550 compression-recovery cycle tests (**Fig. S15**), the resistance variation is rapid and stable, remaining nearly constant throughout the testing process. **Fig.s S16(a, b)** illustrate that during significant body deformations, such as bending at the wrist and elbow joints, $\Delta R/R_0$ increases rapidly. As the bending angles of the joints reach 15°, 45°, and 90°, the strength of the electrical signal synchronously enhances. Higher curvature corresponds to greater responsiveness. When the sensor is adhered to the cheek, it can recognize different phonations (**Fig. S16c**).

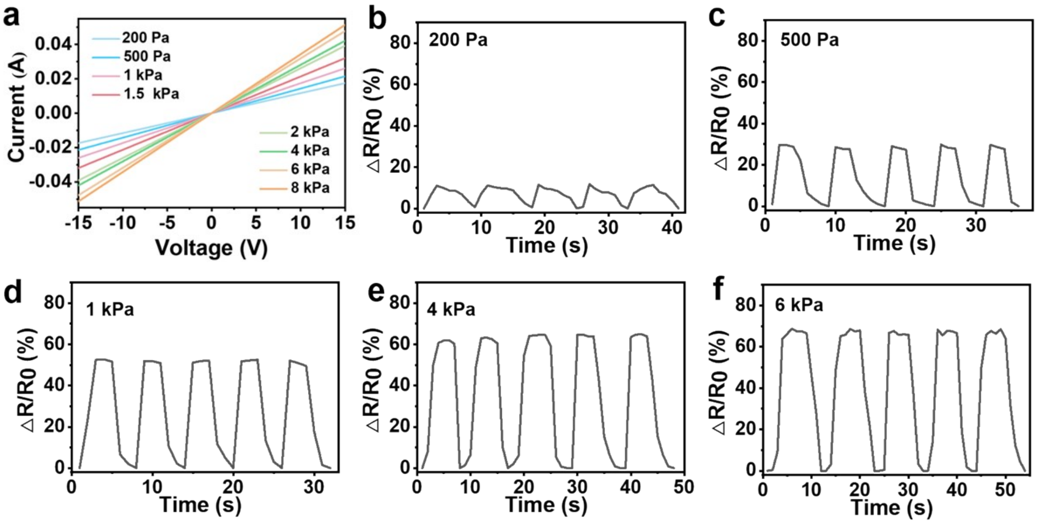

**Fig. S14.** (a) Current-voltage curves under a strain range from 200 Pa to 8 kPa for p-MXene@WPU/BC film sensor. (b-f) Real-time relative resistance changes ($\Delta R/R_0$) of p-MXene@WPU/BC film sensor in response to different stress.

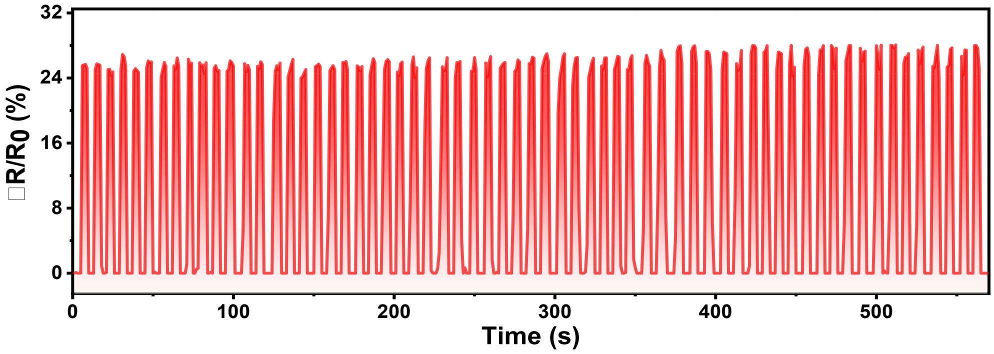

**Fig. S15.** Cyclic stability test after performing a cycle up to five thousand times at a 1 kPa pressure on p-MXene@WPU/BC film.

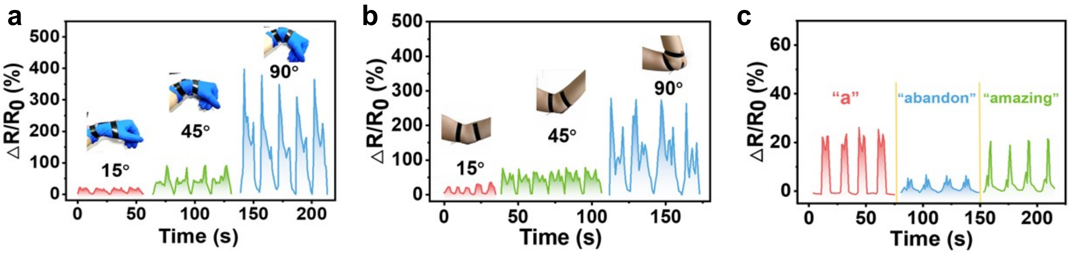

**Fig. S16.** Changes in the electrical signals of the p-MXene@WPU/BC composite film sensor corresponding to different states of motion: (a) wrist bending and (b) elbow bending at different amplitudes. (c) Different words correspond to changes in electrical signals.

### 1.6 Dynamic relationship between sensing and electromagnetic shielding

In order to realize the study of the dynamic interaction between electromagnetic shielding (EMI) and sensing properties of the films, we first applied a controlled tensile strain to the films. Subsequently, the films were immobilized using a fixture to ensure that they maintained a constant tensile state throughout the EMI shielding measurements. Through this approach, we were able to systematically investigate the changes in the EMI shielding effectiveness and its sensing performance of the films under different strain conditions. Through this approach, As shown in **Fig. S17**, we successfully evaluated the dynamic changes in EMI shielding effectiveness (SE) under mechanical deformation.

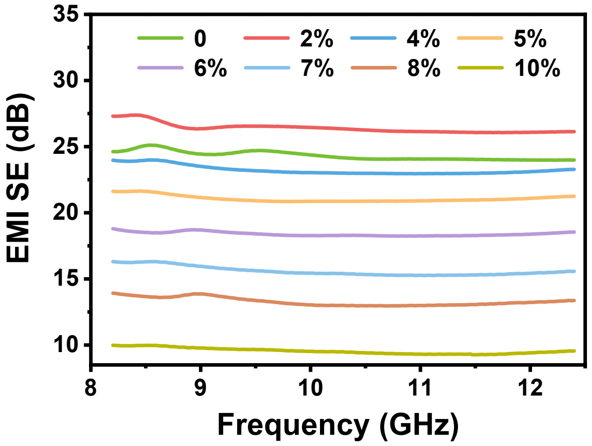

**Fig. S17.** Electromagnetic shielding performance curves of p-MXene@WPU/BC film with different tensile strains.

**Table S2.** Key performances of the p-MXene@WPU/BC-based sensors in comparison with reported literature.

| Materials | Form | Key performances | | | | Ref. |
|---|---|---|---|---|---|---|
| | | Mechanical property | Electromagnetic shielding | Stress sensitivity (0~5 kPa) | Strain sensing | |
| MXene/BC | film | 250 MPa/10% | - | 51.14 | - | 20 |
| Ag/ANFs@BC | film | 58.3 MPa/11% | - | - | √ | 21 |
| BC/MWCNT | aerogel | 37 MPa/16% | - | - | √ | 22 |
| Silver Nanowire/BC | fiber | 198 MPa/3% | - | 33.96±0.5 | - | 23 |
| BC/PPy-P | fiber | 500 MPa/2.5% | - | - | √ | 24 |
| LiTFSl/TOBC | hydrogel | 0.85 MPa/3100% | - | - | √ | 25 |
| BC/PPy@EF | hydrogel | 13.29 N/528.98% | - | - | √ | 26 |
| cPPy/BCNF | hydrogel | 9 MPa/350% | - | - | √ | 27 |
| $ImClO_4$/BC | hydrogel | 21 MPa/18.5% | - | 5.49 | - | 28 |
| $Ti_3C_2T_x$/BC | film | 300 MPa/10% | 40 dB | - | - | 29 |
| **p-MXene@WPU/BC** | **film** | **340 MPa/11%** | **72 dB** | **40.48** | √ | **This work** |

## 1. Captions for Movies

**Supplementary Movie S1:** The performance of the thin-film electrochromic device was examined under the application of 15 V. The results demonstrated the device's capacity to reliably and consistently undergo colour changes.

**Supplementary Movie S2:** Repeated twisting and folding possible. The results show that the device has good flexibility.

**Supplementary Movie S3:** Repeated stretching of a 3 kg dumbbell. The results show that the device has excellent mechanical strength.

**Supplementary Movie S4:** Observe the change in bulb brightness under finger pressure. The results demonstrate the potential of the device for pressure sensing.

### 3. Reference

1 J. Orangi, F. Hamade, V. A. Davis and M. Beidaghi, *ACS Nano*, 2020, **14**, 640–650.
2 S.-H. Hwang, D. Kang, R. S. Ruoff, H. S. Shin and Y.-B. Park, *ACS Nano*, 2014, **8**, 6739–6747.
3 L. Jiao, H. Xiao, Q. Wang and J. Sun, *Polym. Degrad. Stab.*, 2013, **98**, 2687–2696.
4 A. Santamaria-Echart, L. Ugarte, C. García-Astrain, A. Arbelaiz, M. A. Corcuera and A. Eceiza, *Carbohydr. Polym.*, 2016, **151**, 1203–1209.
5 L. Urbina, A. Alonso-Varona, A. Saralegi, T. Palomares, A. Eceiza, M. Á. Corcuera and A. Retegi, *Carbohydr. Polym.*, 2019, **216**, 86–96.
6 Z. Zhan, Q. Song, Z. Zhou and C. Lu, *J. Mater. Chem. C*, 2019, **7**, 9820–9829.
7 H. Liu, Z. Cui, L. Luo, Q. Liao, R. Xiong, C. Xu, C. Wen and B. Sa, *Chem. Eng. J.*, 2023, **454**, 140288.
8 Z. Ling, C. E. Ren, M.-Q. Zhao, J. Yang, J. M. Giammarco, J. Qiu, M. W. Barsoum and Y. Gogotsi, *Proc. Natl. Acad. Sci.*, 2014, **111**, 16676–16681.
9 W.-T. Cao, F.-F. Chen, Y.-J. Zhu, Y.-G. Zhang, Y.-Y. Jiang, M.-G. Ma and F. Chen, *ACS Nano*, 2018, **12**, 4583–4593.
10 F. Moglie, D. Micheli, S. Laurenzi, M. Marchetti and V. Mariani Primiani, *Carbon*, 2012, **50**, 1972–1980.
11 L. Zhang, M. Liu, S. Roy, E. K. Chu, K. Y. See and X. Hu, *ACS Appl. Mater. Interfaces*, 2016, **8**, 7422–7430.
12 K. Ji, H. Zhao, J. Zhang, J. Chen and Z. Dai, *Appl. Surf. Sci.*, 2014, **311**, 351–356.
13 L. Kong, X. Yin, M. Han, X. Yuan, Z. Hou, F. Ye, L. Zhang, L. Cheng, Z. Xu and J. Huang, *Carbon*, 2017, **111**, 94–102.
14 Z. Chen, C. Xu, C. Ma, W. Ren and H.-M. Cheng, *Adv. Mater.*, 2013, **25**, 1296–1300.

15 W.-L. Song, X.-T. Guan, L.-Z. Fan, W.-Q. Cao, C.-Y. Wang, Q.-L. Zhao and M.-S. Cao, *J. Mater. Chem. A*, 2015, **3**, 2097–2107.

16 N. Agnihotri, K. Chakrabarti and A. De, *RSC Adv.*, 2015, **5**, 43765–43771.

17 W.-T. Cao, F.-F. Chen, Y.-J. Zhu, Y.-G. Zhang, Y.-Y. Jiang, M.-G. Ma and F. Chen, *ACS Nano*, 2018, **12**, 4583–4593.

18 M. Han and W. Shen, *Carbohydr. Polym.*, 2022, **298**, 120109.

19 J. Xiong, R. Ding, Z. Liu, H. Zheng, P. Li, Z. Chen, Q. Yan, X. Zhao, F. Xue, Q. Peng and X. He, *Chem. Eng. J.*, 2023, **474**, 145972.

20 T. Su, N. Liu, D. Lei, L. Wang, Z. Ren, Q. Zhang, J. Su, Z. Zhang and Y. Gao, *ACS Nano*, 2022, **16**, 8461–8471.

21 S. Chen, Y. Wang, B. Fei, H. Long, T. Wang, T. Zhang and L. Chen, *Chem. Eng. J.*, 2022, **430**, 131980.

22 H. Hosseini, M. Kokabi and S. M. Mousavi, *Carbohydr. Polym.*, 2018, **201**, 228–235.

23 F. Guan, Y. Xie, H. Wu, Y. Meng, Y. Shi, M. Gao, Z. Zhang, S. Chen, Y. Chen, H. Wang and Q. Pei, *ACS Nano*, 2020, **14**, 15428–15439.

24 Z. Yuan, H. Yin, M. Zheng, X. Chen, W. Peng, H. Zhou, J. Xing, L. Wang and S. Hu, *Carbohydr. Polym.*, 2025, **349**, 122963.

25 L. Chen, J. Lou, X. Rong, Z. Liu, Q. Ding, X. Li, Y. Jiang, X. Ji and W. Han, *Carbohydr. Polym.*, 2023, **321**, 121310.

26 C. Gao, Y. Liu, F. Gu, Z. Chen, Z. Su, H. Du, D. Xu, K. Liu and W. Xu, *Chem. Eng. J.*, 2023, **460**, 141769.

27 X. Xu, S. Wu, J. Cui, L. Yang, K. Wu, X. Chen and D. Sun, *Compos. Part B-Eng.*, 2021, **211**, 108665.

28 J. Lu, S. Hu, W. Li, X. Wang, X. Mo, X. Gong, H. Liu, W. Luo, W. Dong, C. Sima, Y. Wang, G. Yang, J.-T. Luo, S. Jiang, Z. Shi and G. Zhang, *ACS Nano*, 2022, **16**, 3744–3755.

29 Y. Wan, P. Xiong, J. Liu, F. Feng, X. Xun, F. M. Gama, Q. Zhang, F. Yao, Z. Yang, H. Luo and Y. Xu, *ACS Nano*, 2021, **15**, 8439–8449.